PCCP

ROYAL SOCIETY OF CHEMISTRY

PAPER

View Article Online
View Journal | View Issue

Cite this: *Phys. Chem. Chem. Phys.*, 2026, **28**, 3236

2D correlation SERS of organic ions using AuNP films at electrified soft interfaces

Madjid Tarabet,[a] Yinxi Zou,[a] Dyia Syaleyana Md Shukri,[abc] Noorfatimah Yahaya,[c] Manuel Dossot*[a] and Grégoire Herzog*[a]

This study reports the formation of gold nanoparticle (AuNP) films by electrochemical assembly at the polarized water|trifluorotoluene interface (ITIES) and their use as SERS substrates whose activity can be tuned by the interfacial potential. Using a four-electrode configuration, cyclic modulation of the interfacial potential induced the growth of AuNP films, monitored in real time by total internal reflection (TIR) UV-Vis spectroscopy. The absorbance evolution reveals two distinct growth regimes, while the interfacial double-layer capacitance (C_{dl}) increases steadily with the number of cycles. These electrochemically generated films were subsequently evaluated as SERS-active substrates for two cationic probes: methylene blue (MB^+) and norfloxacin (Nor^+). The interfacial potential governs their adsorption and distribution between the phases. To discriminate spectral responses and identify the sequence of interfacial processes as a function of applied potential, two-dimensional correlation spectroscopy using the applied potential as the external perturbation of the system was employed. The synchronous and asynchronous maps highlight potential-induced changes in adsorption states as well as competitive interactions between the probe molecules, the supporting electrolyte and the AuNPs film at the interface. Overall, these results demonstrate that electrochemically assembled AuNP films act as dynamic plasmonic substrates whose SERS performance can be modulated by potential (EC-SERS), while 2D-Correlation Spectroscopy provides a complementary approach to unravel multi-species mechanisms at liquid–liquid interfaces.

Received 10th November 2025,
Accepted 11th January 2026

DOI: 10.1039/d5cp04332h

rsc.li/pccp

Introduction

The interface between two immiscible liquid phases was used for the assembly of nanoparticles offering a reproducible and defect-free surface.[1] Such interfaces can then be used for electrocatalysis,[2,3] mirror-like surfaces[4] and for surface enhanced Raman spectroscopy.[5] Nanoparticles have been assembled at a liquid–liquid interface through different means which include: (i) the addition of solvent[6]; (ii) the addition of an organic molecule, described as a 'promoter'[7]; (iii) the screening of the nanoparticle charge[8,9]; (iv) the centrifugation of a biphasic system.[8] After the addition of oleic acid to an aqueous suspension of Au nanorods, they spontaneously self-oriented at the liquid–liquid interface.[6] The nanorod assembly was then used for the detection of 1,1′-diethyl-2,2′- cyanine, 1,2-bis(4-pyridyl)ethane, and adenine. Another example from the literature includes the addition of malachite green to the biphasic system: aqueous Au nanoparticle suspension|1,2-dichloroethane.[7] After thorough mixing, a gold film was formed with adsorbed malachite green molecules, which resulted in SERS spectra. The third approach to Au nanoparticle assembly is based on the screening of the charges of the nanoparticles leading to the destabilization of the colloidal suspension. The addition of aqueous salts (*e.g.* NaCl) leads to aggregation through the reduction of electrostatic repulsion between nanoparticles.[8,10] The other option is to screen the charge by adding a hydrophobic ion of the opposite charge to the nanoparticle (*e.g.* tetrabutylammonium chloride).[9,11,12] Au nanoparticles assembly formed at liquid–liquid interfaces have been used for the detection of a variety of analytical targets, including organic molecules,[10,13] bacteria,[14] biomolecules,[15] and microplastics.[16] The nanostructures formed can be used for *ex situ*[11–14] or *in situ*[10,15,16] SERS applications. *In situ* SERS presents several advantages, which include (i) keeping the target molecule's integrity; (ii) avoiding local heating caused by the laser beam.

Wang *et al.* have examined the behavior of Au nanoparticle assemblies at the liquid–liquid interface with *in situ* SERS.[17] They have investigated how two molecules 1-dodecanethiol and tetramethyl ammonium have an impact on the film properties, when a monolayer, a 2D film or a multilayer is formed. The analysis of SERS spectra revealed that the Au nanoparticles surface chemistry depended strongly on the chemical environment, which

[a] *Université de Lorraine, CNRS, LCPME, F-54000, Nancy, France. E-mail: manuel.dossot@univ-lorraine.fr, gregoire.herzog@cnrs.fr*
[b] *Department of Toxicology, Advanced Medical and Dental Institute (AMDI), Universiti Sains Malaysia, 13200, Bertam Kepala Batas, Pulau Pinang, Malaysia*
[c] *Faculty of Applied Sciences, Universiti Teknologi MARA (UiTM) Perlis, Kampus Arau, 02600, Arau, Perlis, Malaysia*

resulted in different morphologies of the films formed. The assembly of Au nanoparticles was governed by both electrostatic and hydrophobic interactions and the variation in SERS spectra was the result of the modulation of the chemical environment linked to the tetramethylammonium and 1-dodecanethiol concentrations. However, a fine control over the nanoparticle assembly was difficult to achieve as it depended on parameters such as the surface functionalisation of the nanoparticles, pH of the solution, the concentration of the electrolyte and the presence of any other salts and stabilising compounds present in the aqueous solution such as citrate ions and surfactants.[18] This fine tuning of the Au nanoparticle assembly could be brought by an external driving such as an electric field.

The electrochemical polarization of the liquid–liquid interface, also known as electrochemistry at the interface between two immiscible electrolyte interfaces (ITIES) allowed the control of the distribution of ionic species on both sides of the interface according to their hydro-/lipophilicity and their charge.[19] The formation of Au nanoparticle films was electrochemically induced by the application of a interfacial potential difference.[20–26] Experimental data based on cyclic voltammetry and capacitance studies showed that negatively charged Au nanoparticles adsorb at the negative end of the potential window.[20] Booth *et al.* have investigated *in situ* SERS measurement coupled to electrochemistry (EC-SERS) at the ITIES modified with Ag nanoparticles.[27] After the application of an interfacial potential difference of 0 V for 20 min, the Ag nanoparticles assembly was induced at the interface, leading to a SERS signal of the organic background electrolyte and solvent. The EC-SERS response varied reproducibly with the distance from the interface and with the interfacial potential difference applied.

We propose here to investigate the assembly of Au nanoparticle films through cycling of the potential window. The film formation was followed by total internal reflectance (TIR) visible spectroscopy. The films formed were then used for the study of the EC-SERS signal under electrochemical polarization of the ITIES. Two cationic organic molecules were selected as targets: methylene blue (MB^+) and norfloxacin (Nor^+). EC-SERS at the ITIES may lead to a wealth of information on the chemical composition of the interfacial region, which is dependent of the potential difference applied. 2D correlation spectroscopy is a powerful data visualization tool.[28] It is useful to provide information on the variation of SERS peaks with the changes in applied potential difference. We have used 2D correlation of the SERS data to investigate the impact of interfacial potential difference on the spectra.

Materials and methods

Chemicals and reagents

All chemicals were used without further purification, and all aqueous solutions were prepared using ultrapure water (18.2 MΩ cm, Purelab Option-Q). The glassware was cleaned by soaking it overnight in an oxidizing solution containing 0.1 M potassium permanganate ($KMnO_4$, 99.5%, Prolabo) and 90 mM sulfuric acid (H_2SO_4, Sigma-Aldrich, 95–97%), followed by rinsing with a solution of H_2SO_4 and hydrogen peroxide (H_2O_2, Sigma-Aldrich, 30% w/w) mixed in a 1 : 3 volume ratio. The glassware was then thoroughly rinsed with boiling water and acetone.

The analytes used in SERS measurements at the ITIES interface were methylene blue ($C_{37}H_{27}N_3Na_2O_9S_3$, Fluka) and norfloxacin ($C_{16}H_{18}FN_3O_3$, 98%, Merck). Tetrapropylammonium chloride (TPACl, Sigma Aldrich, 98%) was used as the model species for calibration of the potential window.

The organic electrolytes included bis(triphenylphosphoranylidene)ammonium chloride (BACl, 97%, Sigma-Aldrich) and lithium tetrakis(pentafluorophenyl)borate in diethyl ether (LiTB, Boulder Scientific Company). Bis(triphenylphosphoranylidene)ammonium tetrakis(pentafluorophenyl)borate (BATB) was synthesized by mixing equimolar solutions of BACl and LiTB in a 2 : 1 (v/v) water-to-methanol ratio. The resulting precipitate was filtered, washed, dissolved in acetone, and recrystallized. The crystals were subsequently washed twice with a 1 : 1 (v/v) mixture of water and acetone.

Gold nanoparticles (AuNPs) were synthesized using gold tetrachloride trihydrate ($HAuCl_4$, $3H_2O$ 99.9%, Sigma-Aldrich) and trisodium citrate dihydrate ($Na_3C_6H_5O_7$ $2H_2O$, 99%, Sigma Aldrich) according to the protocol used in our previous publication.[10] The quality of the Au NP batch was checked by UV-vis absorption spectroscopy. The average diameter measured for AuNPs was 20.1 ± 2.3 nm and the AuNP concentration in the colloidal suspension was $C_0 = (1.70 \pm 0.11) \times 10^{11}$ particles per mL or (282 ± 18) pM.

The surface of the electrochemical cell was silanized using a mixture of 20 μL trimethylchlorosilane (98%, Sigma-Aldrich) in 20 mL of TFT (99%, Sigma-Aldrich). The organic solvent employed for the organic phase was α,α,α-trifluorotoluene (TFT, Sigma-Aldrich).

Electrochemistry and AuNP film electrogeneration

Electrochemical experiments were conducted using a four-electrode electrochemical cell setup (Fig. S1) and a custom electrochemical cell for *in situ* and *operando* EC-SERS measurements (Fig. S2). Initially, the electrochemical assembly of AuNPs into a film at the ITIES was achieved using a conventional electrochemical cell equipped with a four-electrode setup. This included two pseudo-reference electrodes made of silver wires coated with silver chloride (Ag/AgCl) and two platinum counter electrodes. AuNP films at the ITIES were formed by cyclic voltammetry (CV) using the following electrochemical cell: Ag|AgCl|C_0/2 AuNP (aqueous)‖2.5 mM BATB in TFT|2.5 mM BACl (aqueous)|Ag|AgCl. The assembly of the AuNP film was induced through repetitive cycling (up to 90 cycles) using a PGSTAT 101 potentiostat (Metrohm, France) at a scan rate of 20 mV s^{-1}. TPA^+ was added to the aqueous phase of the electrochemical cell at the end of a series of experiments for calibration of the potential window. The formal potential of TPA^+ was +0.022 V for an aqueous‖TFT interface.[29]

Total internal reflectance spectroscopy coupled to electrochemical measurements

AuNP film formation was investigated *in situ* using a Total Internal Reflectance set-up. A UV-vis Olympus halogen lamp

was used as a light source and an Avantes spectrophotometer (Avantes AvaSpec ULS-2048) as a detector, equipped with a 2048-pixel array working between 200 nm and 1100 nm. Due to the fact that the lenses used in our home-made set-up are not UV-grade, the working spectral range was between 380 nm and 1100 nm. The spectral resolution was 2 nm. The light emitted was brought to the sample and collected to the detector through an optical path composed of convergent lenses and mirrors shown in Fig. S3. The electrochemical cell was placed on a platform, whose height was finely adjustable with a micrometer head.

Raman spectroscopy

Raman spectroscopy was performed using a Renishaw Qontor confocal Raman microscope equipped with either a 785 nm solid-state laser (500 mW) or a 532 nm solid state laser (200 mW). A 1200 grooves mm^{-1} grating was used. A Peltier-cooled CCD camera was employed for spectral acquisition (temperature set at −70 °C). For solid samples, a ×50 long working distance objective (numerical aperture: 0.50) was used, with laser power reduced to 2–5 mW to avoid sample damage. Typically, spectral acquisition involved averaging 5 spectra with an exposure time of 4 seconds per spectrum and 2 mW laser power. For *in situ* Raman spectroscopy at the polarized aqueous–TFT interface, a × 60 water immersion objective (numerical aperture: 0.90) was employed. The 785 nm laser power was similarly limited to 1% (5 mW) to collect surface-enhanced Raman spectroscopy (SERS) signals under identical acquisition conditions as for solid samples.

2D correlation spectroscopy (2D-COS).

The Raman spectra collected at various applied potentials were converted in text files and treated by the 2D correlation software 2DShige developed by Prof. Shigeaki Morita (Osaka Electro-Communication University) and freely available online (https://sites.google.com/view/shigemorita/home/2dshige). This software allows to obtain both synchronous and asynchronous 2D correlation maps, the applied potential being the perturbation of the system. The correlation maps were exported as text files and used in the Origin software (from OriginLab, https://www.originlab.com/) to plot the results.

Results

Electrochemically induced AuNP films@ITIES

The formation of AuNP film was induced through electrochemical cycling between −0.3 V and + 0.8 V at 20 mV s^{-1} for up to 90 cycles (Fig. 1A). At the end of each cycle, a TIR visible spectrum was recorded (Fig. 1B). These experiments were run for initial concentrations of $C_0/2$ (Fig. 1) and $C_0/3$ (Fig. S4). Although the variation of CVs was hardly perceptible, the double layer capacitance, C_d, of the interface was calculated at $\Delta^{aq}_{org}\phi$ = +0.25 V, based on the experimental data from Fig. 1A, according to eqn (1):

$$C_{dl} = \frac{(i_{forward} - i_{reverse})}{2\nu A} \quad (1)$$

where $i_{forward}$ and $i_{reverse}$ are the forward and reverse currents respectively, ν is the scan rate (in V s^{-1}) and A is the surface area of the interface (in cm^2). The initial capacitance for $C_0/2$ was 31.6 μF cm^{-2} and rose steadily to 45.5 μF cm^{-2}. The double layer capacitance increased with the number of cycles at a faster rate when the initial concentration of AuNPs was greater (Fig. 2A). Indeed, a slope of (0.16 ± 0.01) μF cm^{-2} $cycle^{-1}$ was measured for $C_0/2$ against a slope of (0.10 ± 0.01) μF cm^{-2} $cycle^{-1}$ for $C_0/3$. The Chow test demonstrated that the slopes and the intercepts for the capacitance data as a function of the number of cycles differed significantly for $C_0/2$ and $C_0/3$. The slope for $C_0/2$ is 56% greater than the one for $C_0/3$ indicating that the rate of AuNP accumulation at the interface increased with their initial concentration.

The absorbance measured in TIR mode (Fig. 1B) increased with the number of cycles throughout the wavelength range studied (400 to 700 nm). This increase was very rapid for the first five cycles and then, the absorbance increased steadily at a much lower rate. The trend of the absorbance (λ = 650 nm) as a function of cycles for $C_0/2$ and $C_0/3$ is shown in Fig. S5. It could be explained by two different regime of film formation. At first,

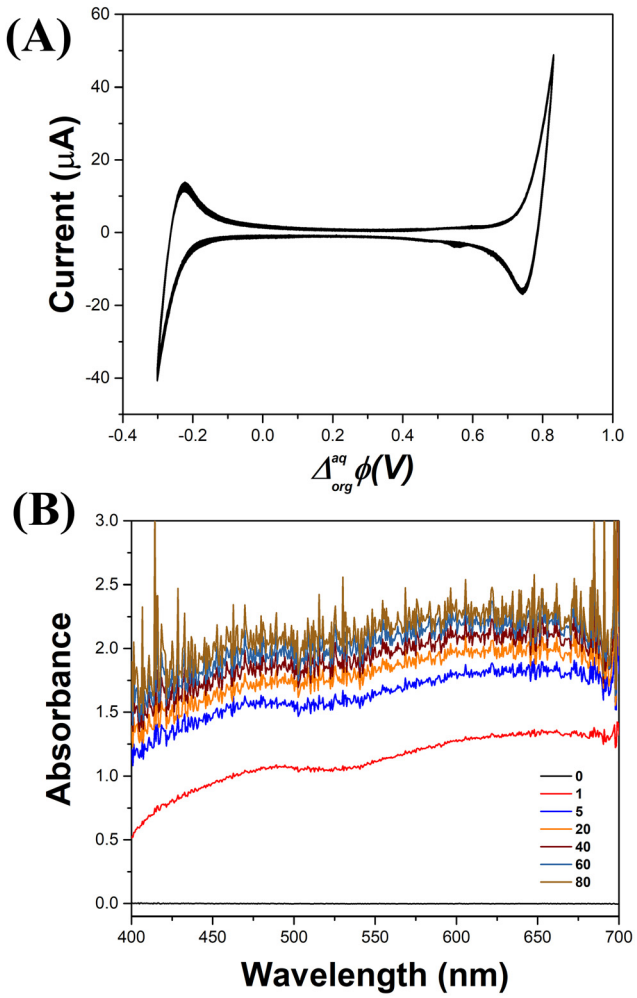

Fig. 1 (A) CV of the electrogeneration of AuNP films with $C_0/2$, ν = 20 mV s^{-1}, 90 cycles. (B) Evolution of absorbance with the number of cycles during the Au NP film electrogeneration by CV. For simplicity, only spectra after cycles 1, 5, 20, 40, 60, and 80 are shown. Black curve represent the absorbance before the electrogeneration of the AuNP film.

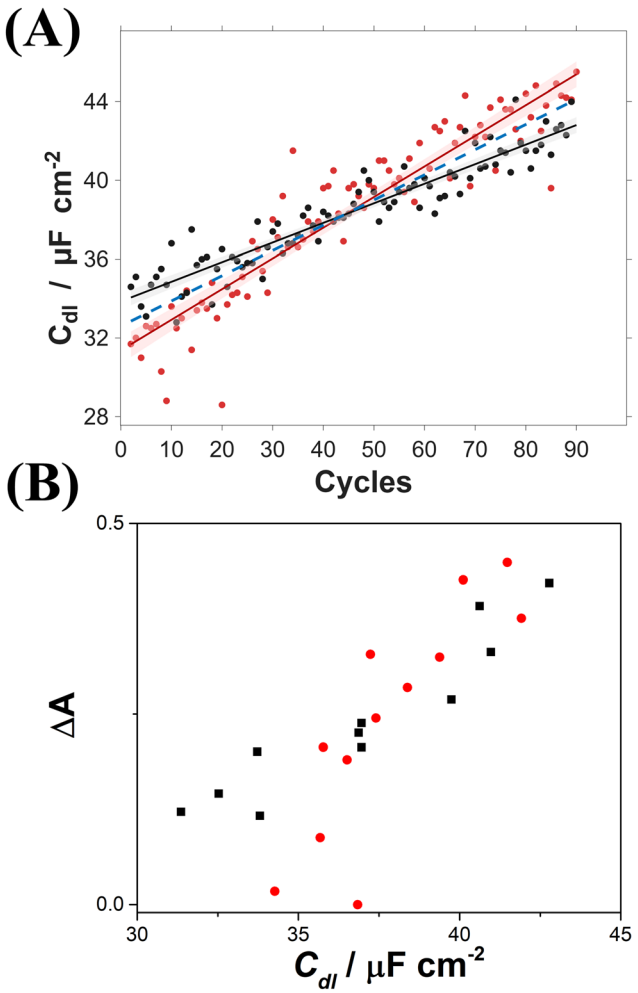

Fig. 2 (A) Evolution of the capacitance double layer as a function of the number of cycles for AuNPs $C_0/2$ (●) and $C_0/3$ (●). The solid represents the linear fitting for $C_0/2$: $y = (0.16 \pm 0.01)x + 62 \pm 1$ and $C_0/3$: $y = (0.10 \pm 0.01)x + 70 \pm 1$. The blue dashed line represents the linear regression for all data points ($C_0/2$ and $C_0/3$). (B) Variation of absorbance, ΔA, of the AuNP film as a function of the double layer capacitance determined from CVs. These data were collected for cycles 10, 13, 15, 20, 25, 30, 35, 40, 50, 60, 70, and 80 for initial concentrations of AuNPs $C_0/2$ (■) and $C_0/3$ (●).

a fast regime would be the formation of numerous clusters of Au NPs across the interface. During the slow regime, these clusters would then rearrange, aggregate and AuNPs would also diffuse from the bulk of the solution to the interface. Furthermore, the absorbance increased faster when the initial colloidal suspension was more concentrated (Fig. S5). These combined data obtained through TIR spectro-electrochemistry at the ITIES showed the continuous assembly of Au nanoparticles through the repetitive potential cycling. Fig. S6 shows the photographs of the electrochemical cell before and after the 90 CVs. Initially, the suspension exhibited a homogeneous red colour, characteristic of the colloidal dispersion of AuNPs in the aqueous phase. After 90 cycles, a gold film became visible at the interface, accompanied by an almost complete decolouration of the aqueous phase. This change reflected the diffusion of AuNPs to the interface and their aggregation, driven by the applied electrochemical cycles and ionic charge transfers across the interface. Once collected, the film was rinsed, dried and analysed by SEM (Fig. S7). It appears from the micrographs that the AuNP film thickness is submicrometric.

It was also visible from the spectra shown in Fig. 1B that the signal-to-noise ratio decreased with the number of scans. The noise has become significant as shown for the 80th cycle. This is due to the fact that most of the light was scattered by the AuNP film formed at the interface, and a very small portion reached the spectrophotometer. Fig. 2 shows the plot of the variation of absorbance, ΔA, as a function of the double layer capacitance. ΔA was calculated as the subtraction of the initial absorbance A_0, from the absorbance of the cycle n, A_n. ΔA increased with C_{dl} in a linear fashion regardless of the AuNPs initial concentration in the aqueous phase. These results indicated that the absorbance data collected were related to the formation of the AuNP film at the ITIES and not the result of events in the bulk of the aqueous phase. It should be noted that only the 10th cycles and higher were plotted, so we considered only the slow regime of film formation as seen in Fig. S5. From now on, all films used for SERS experiments were prepared with $C_0/2$ concentration.

EC-SERS of MB$^+$ and Nor$^+$ at polarised liquid–liquid interfaces

A solution of AuNPs at a concentration of $C_0/2$ was cycled 90 times in the large electrochemical cell (described in Fig. S2) to electrochemically induce the formation of the AuNP film (Fig. S8). Control Raman spectra between 600 and 1700 cm^{-1} were recorded and compared to the electrochemical cell before cycling and also to in the absence of AuNPs in the aqueous phase (Fig. S9). We have selected two organic cations (methylene blue, MB$^+$ and norfloxacin, Nor$^+$) to investigate the influence of the polarization potential on the SERS signal. MB$^+$ is a model cation often used in SERS studies due to its electronic resonance nature, while Nor$^+$ is a fluoroquinolone antibiotics. The cyclic voltammetry behavior of MB$^+$ was shown in Fig. 3. The potential window was scanned in the absence and in the presence of 10 μM of MB$^+$, from negative to positive potentials values at a scan rate of 20 mV s^{-1}. These CVs were recorded in the absence of AuNP film. MB$^+$ showed a pair of peaks, indicating that it transferred reversibly at a potential of $\Delta^{aq}_{org}\phi_{1/2} = -0.10$ V. This corresponded to a Gibbs energy of transfer, $\Delta G_{MB^+}0 = -9.6$ kJ mol^{-1} (Fig. 3A). This value is significantly higher than the value of −20.9 kJ mol^{-1} determined at the water|1,2-DCE interface.[30] The greater ΔG^0 values measured at water|TFT interfaces can be attributed to the lower miscibility of water in TFT than in DCE.[31,32] The CV for Nor$^+$ (Fig. S10A) showed, during the forward scan, a rise in current at the positive end of the potential window. In the reverse scan, a sharp peak at +0.35 V was observed, suggesting an adsorption–desorption type of behavior. These electrochemical experiments allowed the determination of the host phase for the cations as a function of potential. For instance, when $\Delta^{aq}_{org}\phi > \Delta^{aq}_{org}\phi_{1/2}$, cations were preferentially in the organic phase, while for $\Delta^{aq}_{org}\phi > \Delta^{aq}_{org}\phi_{1/2}$, they were located in the aqueous phase. The control of the electrochemical potential allows the tuning of ion distribution on either side of the interface.

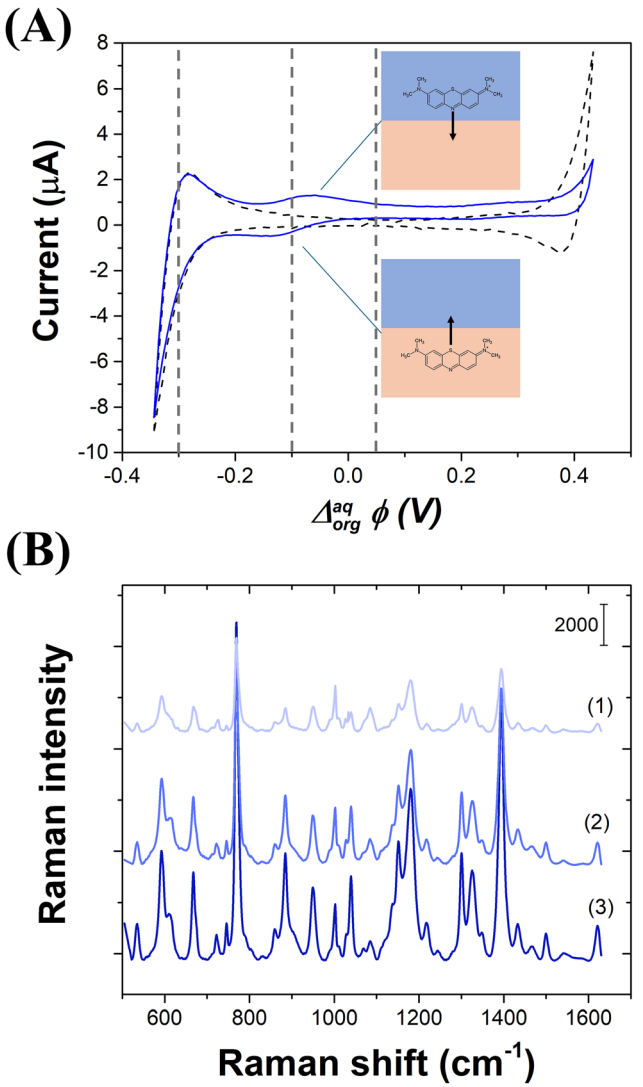

Fig. 3 (A) CV of 10 μM MB^+ at the ITIES. Blank CV is shown as black dashed lines. ν = 20 mV s^{-1}. CVs were recorded in the absence of AuNP film. (B) Average SERS spectra (N = 100) measured at electrogenerated AuNP films for different $\Delta^{aq}_{org}\phi$ values: (1) $\Delta^{aq}_{org}\phi$ = +0.05 V, (2) $\Delta^{aq}_{org}\phi$ = −0.10 V, and (3) $\Delta^{aq}_{org}\phi$ = −0.30 V. These potential values are indicated as dashed lines on (A).

We have investigated the impact of the electrochemical potential difference, $\Delta^{aq}_{org}\phi$, on the SERS signal of MB^+ (Fig. 3B) or Nor^+ cations (Fig. S10B), recorded at an interface modified with a SERS-active gold film formed electrochemically. For each cation, SERS spectra were recorded using the 785 nm laser at the half-wave potential of transfer, $\Delta^{aq}_{org}\phi_{1/2}$, at $\Delta^{aq}_{org}\phi < \Delta^{aq}_{org}\phi_{1/2}$, at $\Delta^{aq}_{org}\phi > \Delta^{aq}_{org}\phi_{1/2}$. In Fig. 3A, the spectra are dominated by the vibration bands of MB^+, due to the electronic resonance. For the experiments with Nor^+ (Fig. S10B), the spectra are dominated by the peaks from the solvent, and the organic background electrolyte although Nor^+ is initially present in the aqueous phase. Since Raman spectra have shown a strong contribution of TFT and BA^+. Data have been normalised to the TFT peak at 769 cm^{-1} to suppress the spectral variance coming from the solvent.

2D correlation spectrum for MB^+ EC-SERS

We have used 2D correlation spectroscopy to help understand the influence of the applied potential to the SERS signal, using the applied potential as the external perturbation of the system.[28] We have first obtained the synchronous and asynchronous correlation maps for the Raman spectra obtained with MB^+ cation (Fig. 4). A synchronous 2D correlation spectrum represents the simultaneous changes in Raman intensity along the variation of $\Delta^{aq}_{org}\phi$. It is shown as a contour map on Fig. 4A. The peaks located in the diagonal of the synchronous 2D correlation (also known as autocorrelation peaks or autopeaks) correspond to the strongest variation in Raman intensity, while Raman peaks of constant intensity or with small changes do not show significant autopeaks. The autocorrelation spectrum (shown in Fig. S11) compared to the conventional Raman spectrum of MB^+ in a suspension of Au nanoparticles. The good agreement between the two spectra confirmed that most of changes in Raman spectra were due to MB^+. A notable exception was the peak at 1624 cm^{-1}, which was almost absent in the slice spectrum while visible in the spectra of Fig. 4A. This peak did not contribute significantly to the spectral variation as the potential was changed, while the peak at 770 and 1395 cm^{-1} were the most variable ones. This may be a good indication that the geometry of the surface adsorption state of MB^+ cation can change at the surface of the gold film when the potential is increased. Correlation squares indicated a positive synchronous correlation between the peaks 593, 770, 884, 1180, 1302, 1328, and 1392 cm^{-1}, meaning that the peaks were either increasing or decreasing together as a function of the variation of $\Delta^{aq}_{org}\phi$. The spectra in Fig, 3B indicated that the Raman intensity of the characteristic MB^+ peaks decreased with the value of $\Delta^{aq}_{org}\phi$. A remarkable aspect of the spectra was the relative intensity of the peaks at 770 and 1392 cm^{-1} compared to the intensity of the peak at 1624 cm^{-1}. The Raman active normal modes of vibration of the MB^+ cations were calculated using density functional theory (DFT). The calculated frequencies (Table S1) are in very good agreement with a previous report[33] despite the use of a slightly different orbital basis set. The corresponding vibrational modes with displacement vectors are given in Fig. S12 for the three Raman peaks at 770, 1392 and 1624 cm^{-1}. The peak at 770 cm^{-1} corresponded to a normal mode involving a distance change of the N and S atoms of the central ring of MB^+. This peak was the most variable with the electric potential applied to the interface (see the autocorrelation spectrum of Fig. S10). We therefore make the hypothesis that at low values of $\Delta^{aq}_{org}\phi$, the MB^+ cation is adsorbed mainly through the interaction of the nitrogen lone pairs of electrons.[33] However, when the potential became close or higher than $\Delta^{aq}_{org}\phi_{1/2}$, the sulphur atom might be involved in the adsorption and changed the polarizability tensor of the molecule, leading to strong Raman intensity of the peak at 770 cm^{-1}. This change of geometry might also affect the peak intensity at 1392 cm^{-1} since this mode involves symmetric CH_3 angular deformation of the methyl groups linked to the exterior nitrogen atoms, close to the sulphur atom.

The variation of intensity in asynchronous 2D correlation spectrum represents the not simultaneous, sequential or successive changes of signal intensities as a function of the interfacial potential difference, *i.e.* the Raman peaks do not reach their maximum intensity at the same potential.[28] The asynchronous correlation spectrum for the MB^+ transfer at the liquid-interface is shown in Fig. 4B. Four Raman peaks at 618, 662, 1001 and 1110 cm^{-1} (marked as vertical dashed red line on Fig. 4B) were attributed to BA^+ cation (Fig. S13 and Table S2) and were positively correlated with the peaks at 770, 884, 1180, 1302, 1328, and 1392 cm^{-1} (attributed to MB^+ and marked as horizontal green dashed lines, Fig. 4B). The positive correlation meant that, when $\Delta^{aq}_{org}\phi$ increased, the intensity of the SERS bands attributed to BA^+ decreased and then the intensity of bands attributed to MB^+ decreased. The positive correlation between SERS bands of the background electrolyte cation, BA^+, and MB^+ was the result of their electrochemical behaviour at the ITIES. Such asynchronous correlation provided information on the chemical environment of the Au films as $\Delta^{aq}_{org}\phi$ varied. When $\Delta^{aq}_{org}\phi < \Delta^{aq}_{org}\phi_{1/2}{}^{MB+}$, MB^+ were adsorbed on AuNPs on the aqueous side of the interface, while BA^+ cations were accumulated on the organic side of the interface. When $\Delta^{aq}_{org}\phi > \Delta^{aq}_{org}\phi_{1/2}{}^{MB+}$, BA^+ diffused from the vicinity of the interface to the bulk of the organic phase, while MB^+ transferred across the interface and also diffused to the bulk.

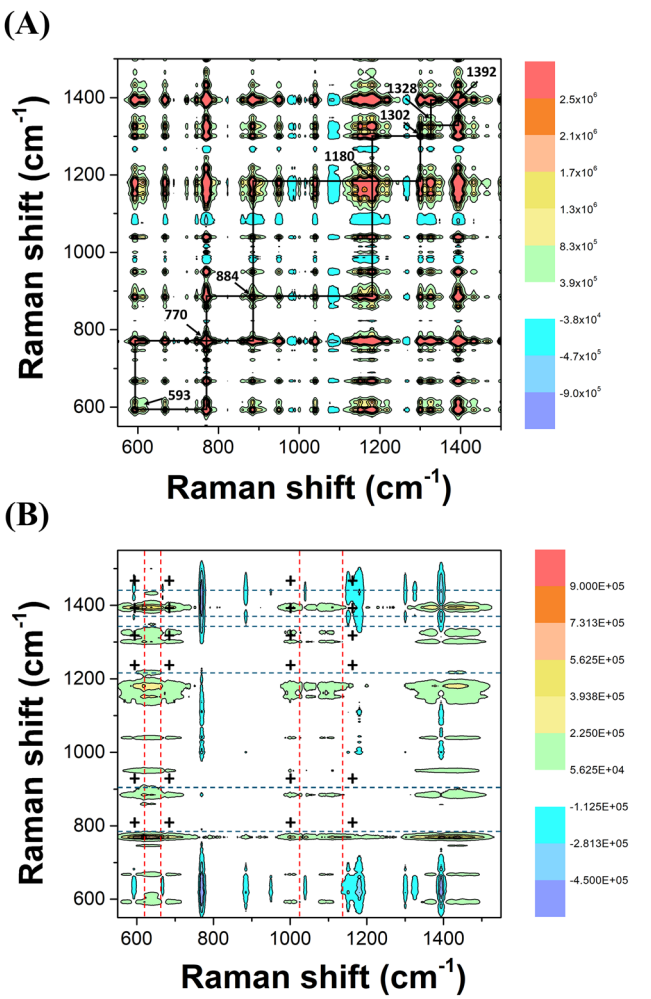

Fig. 4 Synchronous (A) and asynchronous (B) 2D correlation of the SERS spectra (data from Fig. 3A). (A) The squares represent positive correlations between the most prominent peaks, and the dotted line symbolises the autocorrelation spectrum. (B) The vertical dashed lines represent the peaks of the background electrolyte, whereas the horizontal lines represent the ones from MB^+. The '' +'' signs are symbolising the asynchronous positive correlations between the Raman peaks of BA^+ and the ones of MB^+.

2D correlation spectrum for Nor^+ EC-SERS

When considering the EC-SERS data for Nor^+, synchronous 2D correlation spectrum is zoomed in two spectral regions: 600–1150 cm^{-1} (Fig. 5A), and 1150–1630 cm^{-1} (Fig. 5B). When considering the 600–1150 cm^{-1} region, four peaks at 685, 1002, 1027, and 1112 cm^{-1} were considered. These peaks were positively correlated to one another, as shown by the correlation squares (a), (b), and (c) (symbolised in dashed white lines in Fig. 5A). The comparison of the autocorrelation spectrum with spectra of Nor^+ and BA^+ (Fig. 5C) showed that all four peaks can be attributed to BA^+. They represented the strongest spectral variation *vs.* $\Delta^{aq}_{org}\phi$ from the auto-correlation spectrum. In the second spectral region considered (1150–1630 cm^{-1}), two auto-correlation peaks of much smaller intensity at 1269 and 1390 cm^{-1} were positively correlated with one another as shown by the correlation square (a) shown in Fig. 5B. The comparison of the auto-correlation spectrum to the Raman spectra of BA^+ and of Nor^+ helped attributing the auto-correlation peaks at 1269 and 1390 cm^{-1} to Nor^+ (Fig. 5D). Positive correlation indicated that (i) the auto-correlation peaks of BA^+ grew or decreased together with the effect of potential and (ii) and so did the auto-correlation peaks of Nor^+. The full synchronous 2D correlation mapping allowed the determination of the correlation sign between the auto-correlation peaks BA^+ and those of Nor^+ (Fig. S15). The peak of BA^+ at 1002 cm^{-1} was negatively correlated to the one of Nor^+ at 1392 cm^{-1} (correlation square (a), Fig. S15). Furthermore, the peaks from in the region 735–800 cm^{-1} were negatively correlated with the BA^+ at 1002 and 1027 cm^{-1} (correlation square (b), Fig. S13). These observations meant that the signals for BA^+ decreased when the ones for Nor^+ increased (and reversely). The theoretical Raman spectrum for Nor^+ was calculated by DFT (Fig. S14) and the assignment of the Raman peaks for the 1250–1450 cm^{-1} region is shown in Table S3). The vibration modes calculated for this region (1260, 1295, 1337, 1368, 1378, and 1412 cm^{-1}) were linked to phenyl ring deformation in association with the rocking (1260 cm^{-1}) twisting (1295, 1368, and 1378 cm^{-1}), and the wagging (1412 cm^{-1}) of the secondary amino group $-NH_2{}^+$. The Raman band at 1337 cm^{-1} is the only band not associated with vibration of the amino group $-NH_2{}^+$. Since the potential difference determined the ion distribution on either side of the interface, and that the NH_2 group is positively polarized, vibrational modes (at 1260 cm^{-1} and 1375–1420 cm^{-1} region) incorporating its motion are expected to exhibit sensitivity to changes in interfacial polarization. It should be noted that only slight variation in the SERS spectra were observed through the

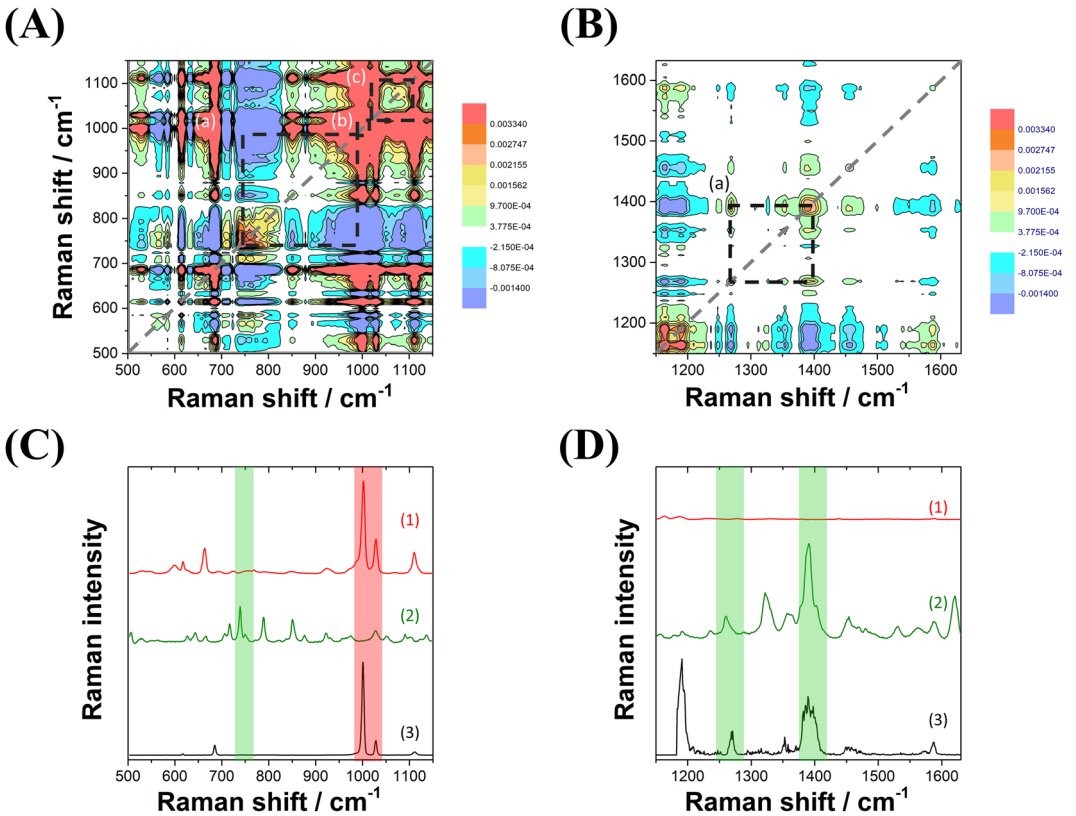

Fig. 5 (A) and (B) Synchronous 2D correlation of the SERS spectra (data from Fig. S10B) in the (A) 550–1150 and (B) 1150–1650 cm^{-1} regions. The squares, noted (a), (b), or (c) represent positive correlations between the most prominent peaks, and the dotted line symbolises the autocorrelation spectrum. (C) and (D) Comparison of the Raman spectra of the liquid–liquid interface (1) and of Nor^+ powder (2) with the autocorrelation spectrum (3) extracted from the synchronous correlation (A) and (B).

autocorrelation spectrum, in line with changes of ion distribution and of the Nor^+ solvation shell.

Asynchronous 2D correlation spectrum is shown in Fig. 6 for the region 900–1500 cm^{-1}. The peaks for BA^+ are represented as horizontal dashed lines at 1002, 1027, and 1112 cm^{-1}, whereas Nor^+ peaks are represented by vertical lines (1269 and 1392 cm^{-1}). The Nor^+ peaks are positively correlated with BA^+ peaks, according to the asynchronous mapping (Fig. 6). Since the correlation between BA^+ and Nor^+ peaks was negative on the synchronous map (Fig. S15), Noda's rule should be reversed.[28] This meant that the decrease of BA^+ peak intensity occurred at lower potentials than the increase of Nor^+ peaks. When the electric potential increased, Nor^+ cations also transferred across the interface and adsorbed on the gold film, leading to strong spectral variance.

Conclusions

Free-floating AuNP films were formed at a polarised liquid–liquid interface under repetitive cycling of the potential window. *In situ* TIR measurements allowed the monitoring of the film formation using two different AuNP concentrations. The absorbance evolution reveals two distinct growth regimes, while the interfacial double-layer capacitance (C_{dl}) increased steadily with the number of cycles. Such films were SERS active towards the organic background electrolyte, BA^+, and other organic cations such as the model molecule, MB^+, and the antibiotic Nor^+. SERS signals varied with the interfacial

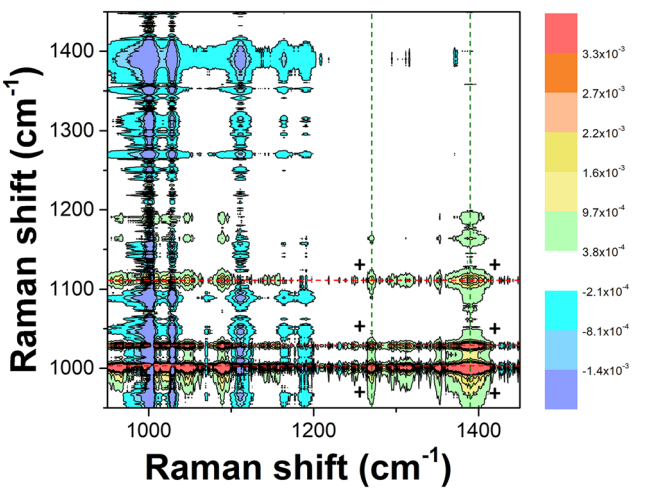

Fig. 6 Asynchronous 2D correlation of the SERS spectra (data from Fig. S10B). The vertical dashed lines represent the peaks of Nor^+, whereas the horizontal lines represent the ones from the background electrolyte. The "+" signs are symbolising the asynchronous positive correlations between the Raman peaks of BA^+ and the ones of Nor^+.

potential applied, $\Delta^{aq}_{org}\phi$. The SERS signal for MB^+ was of much higher intensity than the ones obtained for BA^+ and Nor^+. Indeed, adsorbed MB^+ cations, unlike Nor^+, gave rise to electronic enhanced SERS at 785 nm, hence increasing the SERS cross-section. However, in spite of the low concentration of a non-resonant Nor^+ molecule, SERS signal was detected at the AuNP film. The use of 2D correlation spectroscopy with our Raman data allowed the distinction between the peaks of targeted chemical species (MB^+ or Nor^+) from those of the background electrolyte (BA^+). In the case of MB^+, the strongest variation in peak intensity was observed for the peak at 770 cm^{-1}, which mode of vibration involved the nitrogen atom of the central ring. Th way MB^+ is interacting with the AuNP film through the lone pair of the nitrogen atom is the most influenced by the electrochemical potential difference. 2D correlation of the EC-SERS signal allowed an insight of the molecules – AuNP interactions.

Author contributions

Madjid Tarabet: investigation, methodology, visualization, writing – original draft.; Yinxi Zou: investigation, visualization; Dyia Syaleyana Md Shukri: investigation; Noorfatimah Yahaya: writing – review & editing; Manuel Dossot: conceptualization, funding acquisition, validation, visualization, writing – review & editing.; Grégoire Herzog: conceptualization, funding acquisition, validation, visualization, writing – review & editing.

Conflicts of interest

There are no conflicts to declare.

Data availability

Data for this article, including experimental results in electrochemistry, Raman spectroscopy and UV-vis total internal reflectance are available at Recherche Data Gouv repository at https://doi.org/10.57745/ZIJX1Y.

Supplementary information (SI) contains the description of the electrochemical and spectro-electrochemical set-ups, TIR spectroelectrochemical measurements, EC-SERS, 2D correlations, and DFT calculations. See DOI: https://doi.org/10.1039/d5cp04332h.

Acknowledgements

M. T. acknowledges funding from Université de Lorraine for his PhD. This work was partially supported by the interdisciplinary project LUE ''MAT-PULSE'', part of the French PIA project ''Lorraine Université d'Excellence'' (ANR-15-IDEX-04-LUE). The authors are grateful to the Spectroscopy and Microscopy Service Facility (SMI) of LCPME (Université de Lorraine- CNRS, https://www.lcpme.ul.cnrs.fr/equipements/smi/) where the Raman spectroscopy experiments were conducted. D. S. M. D. visit to LCPME was sponsored by the Embassy of France in Malaysia for Research Mobility Grant 2022. D. S. M. S. gratefully acknowledges Universiti Teknologi MARA (UiTM) and Ministry of Higher Education (MoHE) for awarding her PhD scholarship.

References

1 A. J. G. Zarbin, *Mater. Horiz.*, 2021, **8**, 1409–1432.
2 E. Smirnov, P. Peljo, M. D. Scanlon and H. H. Girault, *ACS Nano*, 2015, **9**, 6565–6575.
3 A. Gamero-Quijano, G. Herzog, P. Peljo and M. D. Scanlon, *Curr. Opin. Electrochem.*, 2023, **38**, 101212.
4 J. B. Edel, A. A. Kornyshev and M. Urbakh, *ACS Nano*, 2013, **7**, 9526–9532.
5 Y. Zhao, L. Shi, Y. Tian and L. Zhang, *Chin. J. Chem.*, 2023, **41**, 569–580.
6 K. Kim, H. S. Han, I. Choi, C. Lee, S. Hong, S.-H. Suh, L. P. Lee and T. Kang, *Nat. Commun.*, 2013, **4**, 2182.
7 M. P. Cecchini, V. A. Turek, J. Paget, A. A. Kornyshev and J. B. Edel, *Nat. Mater.*, 2013, **12**, 165–171.
8 V. A. Turek, M. P. Cecchini, J. Paget, A. R. Kucernak, A. A. Kornyshev and J. B. Edel, *ACS Nano*, 2012, **6**, 7789–7799.
9 Y. Xu, M. P. Konrad, W. W. Y. Lee, Z. Ye and S. E. J. Bell, *Nano Lett.*, 2016, **16**, 5255–5260.
10 M. Tarabet, N. R. Muñoz, M. D. Scanlon, G. Herzog and M. Dossot, *J. Phys. Chem. C*, 2024, **128**, 7936–7947.
11 W. L. J. Hasi, S. Lin, X. Lin, X. T. Lou, F. Yang, D. Y. Lin and Z. W. Lu, *Anal. Methods*, 2014, **6**, 9547–9553.
12 S. Lin, W. L. J. Hasi, X. Lin, S. Q. G. W. Han, X. T. Lou, F. Yang, D. Y. Lin and Z. W. Lu, *Anal. Methods*, 2015, **7**, 5289–5294.
13 T. Cong, J. Wang, Y. Zhao, D. Zhang, Z. Fan and L. Pan, *Anal. Chim. Acta*, 2021, **1154**, 338323.
14 T. Tian, J. Yi, Y. Liu, B. Li, Y. Liu, L. Qiao, K. Zhang and B. Liu, *Biosens. Bioelectron.*, 2022, **197**, 113778.
15 Z. Huang, P. Liu, X. Lin, Y. Xing, Y. Zhou, Y. Luo and H. K. Lee, *J. Chromatogr. A*, 1674, **2022**, 463151.
16 M. Zhao, R. Guo, J. Leng, S. Qin, J. Huang, W. Hu, M. Zhao and Y. Ma, *Sens. Actuators, B*, 2024, **420**, 136504.
17 M. Wang, Z. Zhang and J. He, *Langmuir*, 2015, **31**, 12911–12919.
18 L. Velleman, L. Scarabelli, D. Sikdar, A. A. Kornyshev, L. M. Liz-Marzán and J. B. Edel, *Faraday Discuss.*, 2017, **205**, 67–83.
19 A. Gamero-Quijano, J. A. Manzanares, S. M. B. H. Ghazvini, P. J. Low and M. D. Scanlon, *ChemElectroChem*, 2023, **10**, e202201042.
20 B. Su, J. P. Abid, D. J. Fermín, H. H. Girault, H. Hoffmannová, P. Krtil and Z. Samec, *J. Am. Chem. Soc.*, 2004, **126**, 915–919.
21 K. Lepková, J. Clohessy and V. J. Cunnane, *Electrochim. Acta*, 2008, **53**, 6273–6277.
22 P. P. Fang, S. Chen, H. Deng, M. D. Scanlon, F. Gumy, H. J. Lee, D. Momotenko, V. Amstutz, F. Cortés-Salazar, C. M. Pereira, Z. Yang and H. H. Girault, *ACS Nano*, 2013, **7**, 9241–9248.

23 M. K. Bera, H. Chan, D. F. Moyano, H. Yu, S. Tatur, D. Amoanu, W. Bu, V. M. Rotello, M. Meron, P. Král, B. Lin and M. L. Schlossman, *Nano Lett.*, 2014, **14**, 6816–6822.
24 G. C. Gschwend, E. Smirnov, P. Peljo and H. H. Girault, *Faraday Discuss.*, 2017, **199**, 565–583.
25 X. Wu, H. Xue, Z. Fink, B. A. Helms, P. D. Ashby, A. K. Omar and T. P. Russell, *Angew. Chem., Int. Ed.*, 2024, **63**, e202403790.
26 B. Zhang, Y. Liao, Y. He, M. Zhao and Y. Ma, *Sens. Actuators, B*, 2024, **406**, 135428.
27 S. G. Booth, D. P. Cowcher, R. Goodacre and R. A. W. Dryfe, *Chem. Commun.*, 2014, **50**, 4482–4484.
28 I. Noda, *Anal. Sci.*, 2007, **23**, 139–146.
29 E. Smirnov, P. Peljo, M. D. Scanlon and H. H. Girault, *Electrochim. Acta*, 2016, **197**, 362–373.
30 M. C. Collins, M. Hébrant and G. Herzog, *Electrochim. Acta*, 2018, **282**, 155–162.
31 A. Trojánek, V. Mareček, J. Langmaier and Z. Samec, *Electrochim. Acta*, 2023, **449**, 142222.
32 S. Jin, L. Yang, S. He, T. Fang, X. Sun, D. Cai, Q. Hu, X. Huang and H. Deng, *Chem. Sci.*, 2025, 5017–5027.
33 S. Dutta Roy, M. Ghosh and J. Chowdhury, *J. Raman Spectrosc.*, 2015, **46**, 451–461.

